



Cite this: *Mater. Adv.*, 2023,
4, 2174

Engineering a manganese-based oxide heterostructure cathode for high-performance aqueous potassium-ion storage†

Zheng Guan,^a Yunan Wang,^a Mingyue Zhang,^a Jie Liu,^b Shuangwen Li,^c Di Guo *^a
and Xiaoxia Liu *^a

Advances in aqueous potassium-ion batteries (APIBs) are hindered by the lack of cathode materials with fast K⁺ transport kinetics and stable structures during K⁺ intercalation/deintercalation. Herein, a birnessite/spinel Mn₃O₄ heterostructure cathode is rationally fabricated via a two-step hydrothermal method for aqueous K⁺ storage. Such structure design provides sufficient heterointerfaces and regulates the electronic structure of the Mn atoms in the material, which greatly facilitates the adsorption of K⁺. Meanwhile, the Mn d_{z²} orbital disrupts the long-range collinear Jahn–Teller order of the pure layered birnessite or spinel Mn₃O₄ phase, leading to the remission of Mn dissolution. Due to these merits, the K_{0.52}MnO₂·0.22H₂O/Mn₃O₄ cathode exhibits a high reversible capacity of 147 mA h g⁻¹ at 100 mA g⁻¹ in mild K₂SO₄ electrolyte, a superior rate capability of 99 mA h g⁻¹ at 2 A g⁻¹, and 91.7% capacity retention after 2000 charge/discharge cycles. This work may provide an efficient strategy for the rational design of heterostructures and suppressing the dissolution of Mn to obtain high-performance cathodes for APIBs.

Received 2nd March 2023,
Accepted 31st March 2023

DOI: 10.1039/d3ma00099k

rsc.li/materials-advances

1. Introduction

With a global push towards electric transportation and smart grids, it is crucial to develop large-scale, sustainable and eco-friendly electrochemical energy storage devices with high energy/power density.^{1–6} It is known that lithium-ion batteries are currently the most widely used energy storage devices, but further applications of lithium-ion batteries have been restricted by the limited lithium resource.^{7–10} Among the next-generation rechargeable batteries, aqueous potassium-ion batteries (APIBs) have attracted attention due to their high voltage plateau, low-cost and high safety. However, the potassium storage mechanism is mainly based on the intercalation reaction. Due to the large radius and poor transport mechanics of potassium ions, it often becomes a bottleneck restricting the further breakthrough of cathode performance.^{11–19}

Among the cathode materials for APIBs, the Prussian blue material with large channels for intercalation/deintercalation

of ions is the first choice, as shown in Chart 1.^{20–28} Nevertheless, vacancy defects that exist in the Prussian blue structure result in the reduction of its structural stability and the interruption of electron transport channels, further leading to the deterioration of cyclic stability and the low reversible capacity.^{29,30} Therefore, it is necessary to explore the promising alternative cathode materials. Among many candidates, manganese oxides (including MnO₂, Mn₂O₃, Mn₃O₄, *etc.*) with various phase structures (layered structure, spinel, tunnel phases, *etc.*) and rich polymorphs (α -MnO₂, β -MnO₂, δ -MnO₂, *etc.*) show high electrochemical activity and bright development prospect. These structure characteristics endow Mn-based oxide materials with varying electrochemical properties and potential applications in APIBs.^{31–35} Unfortunately, the Mn-based oxides usually suffer from rapid capacity fading because of Mn dissolution. So far, the corrosion from electrolytes has been widely accepted as being responsible for Mn dissolution upon cycling, during which high-valence Mn cations can be readily reduced to Mn³⁺ or even Mn²⁺ as a result of charge compensation involving Mn. In addition, the well-known Jahn–Teller effect in Mn³⁺ also facilitates Mn dissolution by forming Mn²⁺ via the disproportionation reaction of Mn³⁺ (Mn⁴⁺ + e⁻ → Mn³⁺; 2Mn³⁺ → Mn⁴⁺ + Mn²⁺).^{36,37}

With the Mn dissolution mechanisms verified by many research works, various strategies have been gradually developed, including surface modification, atom doping, ion or molecule

^a Department of Chemistry, Northeastern University, Shenyang, 110819, China.
E-mail: guodi@mail.neu.edu.cn, xxliu@mail.neu.edu.cn

^b School of Resources and Civil Engineering, Northeastern University, Shenyang, 110819, China

^c School of Materials Engineering, North China Institute of Aerospace Engineering, Langfang, 065000, China

† Electronic supplementary information (ESI) available. See DOI: <https://doi.org/10.1039/d3ma00099k>



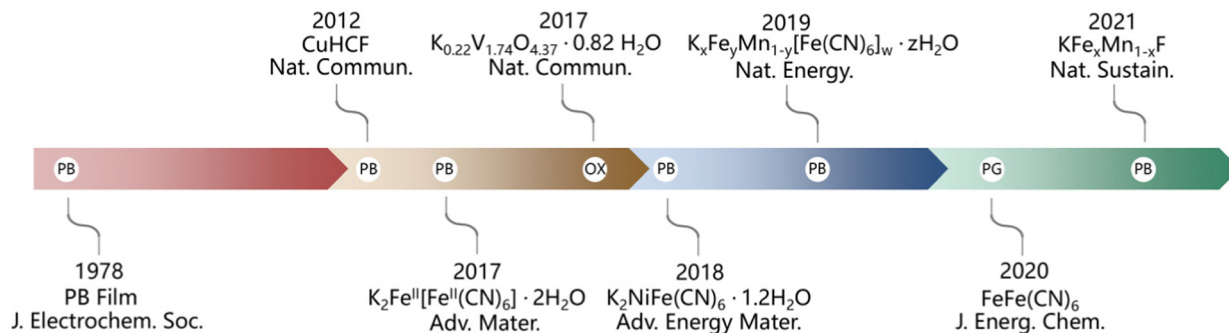


Chart 1 Main progress in cathode materials of aqueous potassium ion batteries.

pre-intercalation, electrolyte optimization and so on.^{38–45} Lu and his colleagues fabricated a potassium manganese hexacyanoferrate cathode featuring an *in situ* cation engineered surface where iron is substituted for manganese. This alternative strategy could reduce the dissolution of manganese and improve the stability of the electrode structure and surface chemical properties.²⁵ Zhang's group prepared a layer of Al_2O_3 coating on the surface of the manganese-based material through atomic layer deposition, as a protective shell alleviating the dissolution of manganese.⁴³ Although these reported works can increase the stability of Mn-based materials markedly, some new problems such as reducing the capacity of Mn active components, sacrificing energy density and complex preparation processes are raised. Therefore, it is crucial to design manganese based materials with a highly stable structure through simple and feasible approaches under the premise of ensuring capacity.

Recently, researchers have discovered that fabricating heterostructures is beneficial to maintain the stability of the structure. Moreover, heterostructure electrodes usually have high reversible capacity, some of which even broke through the theoretical capacity limit.^{46–48} Heterostructures are formed from different semiconductor materials with a similar crystal configuration, atomic spacing and thermal expansion coefficients. The introduction of a heterojunction can change the charge distribution of different chemical compositions due to various band structures, carrier concentrations and Fermi energy levels.^{49–51} Zou *et al.* synthesized $\text{MnO}/\text{Mn}_2\text{O}_3$ for Li-ion battery energy storage, which showed high stability and high rate capability during 10 000 charge/discharge cycles.⁴⁷ Fan *et al.* synthesized a $\text{NaV}_6\text{O}_{15}/\text{V}_2\text{O}_5$ heterostructure for aqueous zinc-ion batteries, which exhibited high stability after 3000 charge/discharge cycles.⁴⁸ These works demonstrated that heterostructure design can accelerate the ionic kinetic ability, maintain the structure stability and alleviate the collapse of the structure caused by volume change.

Here, a layered birnessite/spinel Mn_3O_4 heterostructure material is fabricated through a two-step hydrothermal method as a cathode material for APIBs. The structure transformation from birnessite to spinel can be realized through the reduction reaction and K-ion intercalation *via* the secondary hydrothermal route. By controlling the time of the secondary

hydrothermal route, the K content, crystal water content and micro-morphology of the manganese-based heterostructure can be regulated. As anticipated, the heterostructure at the interface between the birnessite phase and spinel Mn_3O_4 provides more active sites for K^+ storage and reduces the dissolution of Mn, thereby enhancing the stability of the cathode. Consequently, the specific capacity of the optimized sample KMO-2 ($\text{K}_{0.52}\text{MnO}_2 \cdot 0.22\text{H}_2\text{O} + \text{Mn}_3\text{O}_4$ (50.12%)) could reach 147 mA h g^{-1} at 100 mA h g^{-1} . It is maintained at 91.7% initial capacity after 2000 cycles at a current density of 1 A g^{-1} . The potassium ion storage mechanism has been proposed and discussed using experiments and theoretical calculations. The results provide a viable opportunity for the fabrication of high-performance Mn-based oxide cathodes for high-performance APIBs.

2. Experimental section

2.1 Materials

Potassium permanganate (KMnO_4), potassium hydroxide (KOH) and potassium sulphate (K_2SO_4) were purchased from Sinopharm Chemical Reagent (Beijing) Co., Ltd. Nitric acid (HNO_3) was purchased from Damao Chemical Reagent Factory (Tianjin). All the above reagents were analytically pure and do not require further purification. Carbon cloth was purchased from Fuel Cell Earth (United States).

2.2 Synthesis of pure birnessite (KMO)

The electrode was mainly prepared *via* a two-step hydrothermal route, and the active material was directly grown on the conductive carbon cloth, without the use of any binder and additives. A piece of $3 \times 3 \text{ cm}^2$ carbon cloth was first placed in deionized water and anhydrous ethanol for ultrasound treatment for 15 minutes, respectively. After that the carbon cloth was washed with a large amount of deionized water, and then was dried under vacuum conditions. The dried carbon cloth was immersed in 30 ml 30% HNO_3 for 120 min at 120°C . Then, the wet carbon cloth was placed in 30 mL of 12.4 mmol KMnO_4 solution and the hydrothermal reaction was carried out in a 50 mL PTFE reactor for 300 min at 150°C , followed by vacuum drying at 60°C for 48 h. The dried sample is denoted as KMO.



The sample was directly grown on the carbon cloth substrate with an average loading mass of $2.5 \pm 0.3 \text{ mg cm}^{-2}$.

2.3 Synthesis of a birnessite/spinel Mn_3O_4 heterostructure (KMO-X)

The obtained KMO was immersed in 30 mL of 3 M KOH solution for 120 min, 300 min and 480 min at 205 °C, to prepare heterostructure electrodes denoted as KMO-1, KMO-2 and KMO-3, respectively. The carbon cloth containing active materials can be directly used as the cathode for APBs. During the secondary hydrothermal reaction, there was no significant change in active material loading by weighing the substrate mass before and after the reaction.

2.4 Material characterization

Morphology characterization and elemental analysis were analyzed using a scanning electron microscope (SEM, HITACHI, SU8010, Japan) equipped with an energy dispersive X-ray spectroscopy (EDX) detector and a transmission electron microscope (TEM, JEM-ARM200F, JEOL, Japan). The structure of the samples was characterized by XRD (X Pertpro, Netherlands). X-ray photoelectron spectroscopy (XPS) was performed on an XPS spectrometer (ESCALAB 250Xi, Thermo Scientific Escalab, USA) with Cu-K α radiation ($\lambda = 1.54 \text{ \AA}$) as the excitation source. The data were analyzed using the C 1s peak at 284.8 eV as the reference. The mass percentages of K and Mn in the sample were measured accurately by ICP (Angilent ICPOES730, USA) and the content of crystal water was measured by TG (mettler TG-DSC 3+, USA). Thermogravimetric analysis was performed under a N_2 atmosphere from 25 to 300 °C at a heating rate of $3 \text{ }^\circ\text{C min}^{-1}$.

2.5 Electrochemical measurements

Electrochemical measurements were conducted on a multi-channel electrochemical analyzer (VMP3, Bio-Logic-Science Instruments, France). A series of KMO-X samples were directly used as the working electrode, carbon cloth was used as the counter electrode, and the saturated calomel electrode (SCE) was used as the reference electrode to fabricate a three-electrode system. Electrochemical tests were performed using a VMP3 channel in a saturated potassium sulphate solution in the potential range of 0–1.1 V. Electrochemical impedance spectroscopy (EIS) experiments were conducted in the frequency range from 10 mHz to 100 kHz at the open circuit potential with a perturbation of 10 mV on a CHI 660E electrochemical workstation (CH Instruments Inc.). All electrochemical tests were performed at room temperature.

2.6 Density-functional theory (DFT) details

All spin-polarized DFT computations were performed using the Vienna *ab initio* simulation package (VASP) based on the projector augmented wave (PAW) method. Electron–ion interactions were described using standard PAW potentials. A plane-wave basis set was employed to expand the smooth part of the wave functions with a cut-off kinetic energy of 400 eV. The generalized gradient approximation in the form of

Perdew–Burke–Ernzerhof (PBE) was adopted for the exchange–correlation function. The van der Waals interaction was described *via* the DFT-D3 method.

To study the mechanistic chemistry of surface reactions, the surface was modelled with a slab model. A sufficiently large vacuum region of 15 Å was used to ensure that the periodic images were well separated. During the geometry optimizations, the bottom atoms were fixed at the bulk position when the surface properties were calculated. In this work, the Brillouin-zone integrations were conducted using Monkhorst–Pack grids of special points with a separation of 0.06 \AA^{-1} . The convergence criterion for the electronic self-consistent loop was set to 10^{-5} eV. The atomic structures were optimized until the residual forces were below 0.03 eV \AA^{-1} . The heterostructure interface between birnessite and Mn_3O_4 was used as the active site to simulate the adsorption process for K. It is well known that the active sites near the hetero-interface are more active than others. All adsorptive binding energies (E_{ads}) used in this paper were defined as:

$$E_{\text{ads}} = E_{\text{total}} - (E_{\text{A}} + E_{\text{B}})$$

where E_{total} is the total energy of the adsorbate interacting system and E and E_{p} are the energies of the slab and the isolated adsorbate, respectively.

3. Results and discussion

As illustrated in Fig. 1a, the layered birnessite/spinel Mn_3O_4 heterostructure is fabricated *via* a facile two-step hydrothermal route, featuring a modulated interface where part of the birnessite layered structure is converted into the spinel phase. Firstly, the pristine birnessite nanosheets (denoted as KMO) were grown on the carbon cloth *via* a hydrothermal reaction at 150 °C for 300 min. Subsequently, a secondary hydrothermal reaction in KOH solution at a higher temperature of 205 °C was conducted on KMO. By controlling the reaction times of 120 min, 300 min and 480 min, the samples with various components can be achieved, denoted as KMO-1, KMO-2, and KMO-3, respectively. The morphologies of the samples were characterized by scanning electron microscopy (SEM). In Fig. 1b, birnessite nanosheets were grown uniformly at the surface of carbon cloth. After the secondary hydrothermal process, it is clearly observed that vertically aligned nanosheets in KMO are gradually converted into larger nanosheets with some thin nanowires (Fig. 1c–e). With an increase in the hydrothermal time, more nanowires appeared gradually until most of the nanosheets turned into nanowires in KMO-3. The SEM image in Fig. S1 (ESI†) shows pure Mn_3O_4 nanowires obtained *via* extending the secondary hydrothermal time to 960 min, suggesting that the birnessite phase transformed to the spinel phase during the secondary hydrothermal step.

The XRD patterns of KMO, KMO-1, KMO-2 and KMO-3 are shown in Fig. 2a. The XRD patterns show that the peak intensity of the as-synthesized KMO is weak and similar to that of the amorphous structure, and the broad peak located at 25.5°



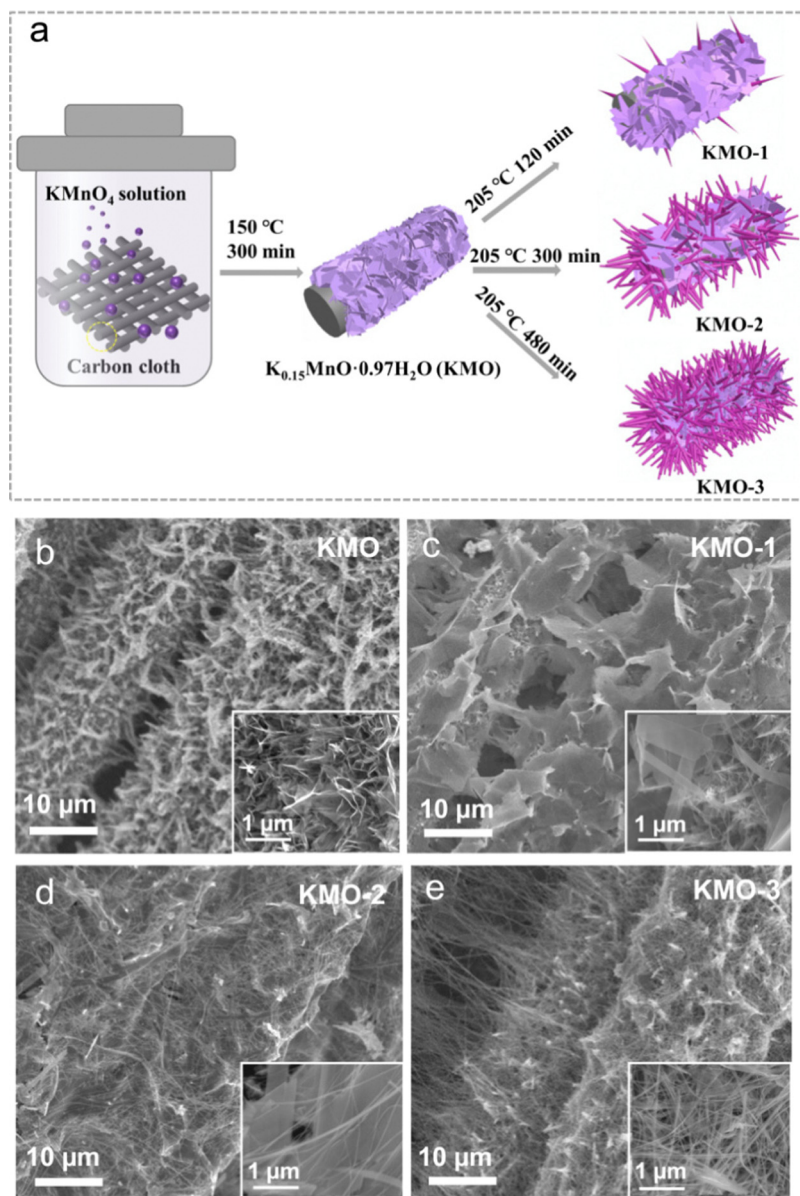


Fig. 1 (a) The illustration of the synthesis process of the Mn-based oxide heterostructure. (b–e) Low magnification SEM images of KMO–KMO-3 samples. Inset: High magnification SEM images of KMO–KMO-3.

is attributed to the carbon cloth substrate. While the XRD characteristic peaks of the KMO-1, KMO-2 and KMO-3 samples correspond to the structure of birnessite (JCPDS No. 80-1098), belonging to the $C2/m$ space group. The diffraction peaks at 12.5° , 25.2° , 37.3° and 42.6° correspond to the (001), (002), (-111) and (-112) planes, respectively. Among these samples, the diffraction peak of KMO-2 is sharp and the intensity is the highest. Notably, the sharp peak at 12.5° is related to the (001) plane of birnessite with a large layer space (0.70 nm) to create sufficient space and accommodation sites for hydrated potassium ions. In the enlarged XRD patterns in Fig. 2b, a small amount of the spinel Mn_3O_4 phase is discovered to emerge gradually in the secondary hydrothermal reaction. This phenomenon suggests that birnessite can be reduced to Mn_3O_4

(JCPDS No. 18-0803) during the secondary hydrothermal reaction process. However for KMO-1 and KMO-3 XRD patterns, it is difficult to distinguish obvious characteristic peaks for the Mn_3O_4 phase. To confirm the phase transition, a control experiment of prolonging the secondary hydrothermal time to 960 min was carried out. The obtained product is proved to be pure spinel Mn_3O_4 based on the XRD spectra (Fig. S2, ESI[†]), indicating the strong reductive effect of carbon cloth in the alkaline environment.³² The component evolution during the two-step hydrothermal process was further investigated by X-ray photoelectron spectroscopy (XPS). The full XPS survey scans of the KMO–KMO-3 samples in Fig. 2c demonstrate the existence of K, Mn, O, and C elements. In Fig. 2d, the binding energy separation (ΔE) difference between the two



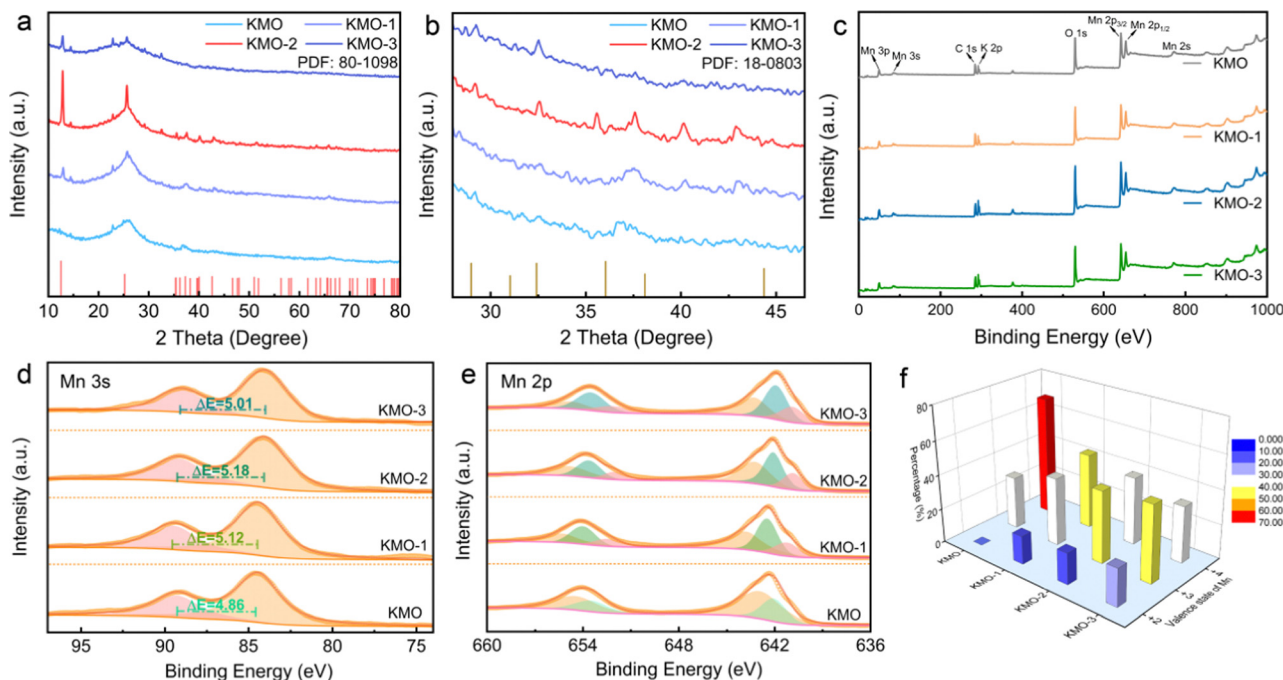


Fig. 2 (a) XRD patterns in the 2θ regions of 10° – 80° for the KMO–KMO-3 samples. (b) XRD patterns in the 2θ region of 25° – 46° for the KMO–KMO-3 samples. (c) XPS spectra of the KMO, KMO-1, KMO-2 and KMO-3 samples. (d) Mn 3s core-level XPS spectra of the KMO–KMO-3 samples. (e) Mn 2p core-level XPS spectra of the KMO–KMO-3 samples. (f) Comparison of different Mn valence (+2, +3 and +4) contents in the KMO–KMO-3 samples.

characteristic peaks of the Mn 3s orbital is 4.86 eV, 5.12 eV, 5.18 eV and 5.01 eV for KMO, KMO-1, KMO-2 and KMO-3, respectively, illustrating that Mn is reduced after the secondary hydrothermal step, which are further supported by the Mn 2p XPS spectra of the four samples. Fig. 2e displays the XPS fitting spectra of Mn $2p_{3/2}$ and Mn $2p_{1/2}$ of KMO, KMO-1, KMO-2 and KMO-3. For KMO, the Mn $2p_{3/2}$ orbital peaks located at 643.0 eV and 642.3 eV are associated with Mn⁴⁺ and Mn³⁺ oxidation. It can be found that the Mn 2p orbital peaks of KMO-1, KMO-2 and KMO-3 moved to the lower binding energy position relative to KMO slightly, revealing that part of Mn⁴⁺ transformed to Mn³⁺ and Mn²⁺ after the secondary hydrothermal reaction. The satellite peak of Mn²⁺ appears at 646.5 eV, further confirming the existence of Mn²⁺. Based on the fitting peak area, the content of Mn⁴⁺, Mn³⁺ and Mn²⁺ in KMO–KMO-3 can be calculated and are shown in Table S1 (ESI[†]). In Fig. 2f, the content of Mn⁴⁺ in the sample reduced dramatically and the content of Mn³⁺ and Mn²⁺ increased gradually with an increase in the secondary hydrothermal reaction time. The TGA curves of KMO–KMO-3 in Fig. S3 (ESI[†]) show that the crystal water contents in KMO, KMO-1, KMO-2 and KMO-3 are estimated to be 3.16, 2.18, 0.36, and 1.94 wt%, respectively (Table S2, ESI[†]). According to the inductively coupled plasma (ICP) measurements, the overall K/Mn atomic ratios for KMO–KMO-3 samples were calculated to be 0.15, 0.17, 0.21, and 0.18, respectively (Table S3, ESI[†]). Therefore, the molecular formulae of KMO, KMO-1, KMO-2 and KMO-3 are determined to be $K_{0.15}MnO_2 \cdot 0.97H_2O$, $K_{0.43}MnO_2 \cdot 1.49H_2O$ (Mn_3O_4 , wt 46.9%), $K_{0.52}MnO_2 \cdot 0.22H_2O$ (Mn_3O_4 , wt 50.1%), and $K_{0.57}MnO_2 \cdot 1.64H_2O$ (wt 54.3%), respectively (Table S4, ESI[†]). It is well-known that birnessite has a sufficient layer space and is

suitable for rapid K⁺ diffusion, but generally limited by low potassium content and much interlayer crystal water. It is difficult to achieve high specific capacity and long cycle life for the birnessite cathode. KMO-2 possesses higher potassium content and lower content interlayer crystal water than KMO, implying the successful intercalation of K⁺ and deintercalation of crystal water during the second-step hydrothermal reaction. During the secondary hydrothermal process, the content of birnessite reduces while more spinel Mn_3O_4 gradually generates, revealing that the manganese in birnessite is reduced to low-valence manganese with the increase of K content. This suggests that the fabrication of heterostructures contributes more electron density changes in Mn⁴⁺, and can be beneficial for rapid alkali-ion intercalation.⁴⁹

The microstructures of KMO–KMO-3 were further investigated by transmission electron microscopy (TEM) in Fig. 3. Fig. 3a–d display the TEM images of the KMO–KMO-3 samples, showing the composites including 2D birnessite nanosheets and 1D Mn_3O_4 nanowire morphology with smooth surfaces. The high-resolution TEM (HRTEM) images are shown in Fig. 3e–h. Clear lattice fringes with interplanar spaces of 0.247, 0.248, 0.247, and 0.248 nm for the (110) plane are observed for KMO, KMO-1, KMO-2, and KMO-3, respectively. The selected area electron diffraction (SAED) illustrates the (110) and (−112) diffraction dots, exhibiting polycrystalline feature and can be well indexed to birnessite. An interlayer distance of 0.67 nm is related to the (001) plane of the birnessite crystal, as shown in Fig. S4 (ESI[†]). Impressively, the HRTEM image of KMO-2 shows two regions with well-resolved lattice fringes with interplanar spacings of 0.247 nm and 0.153 nm, corresponding to the (110) plane of birnessite and



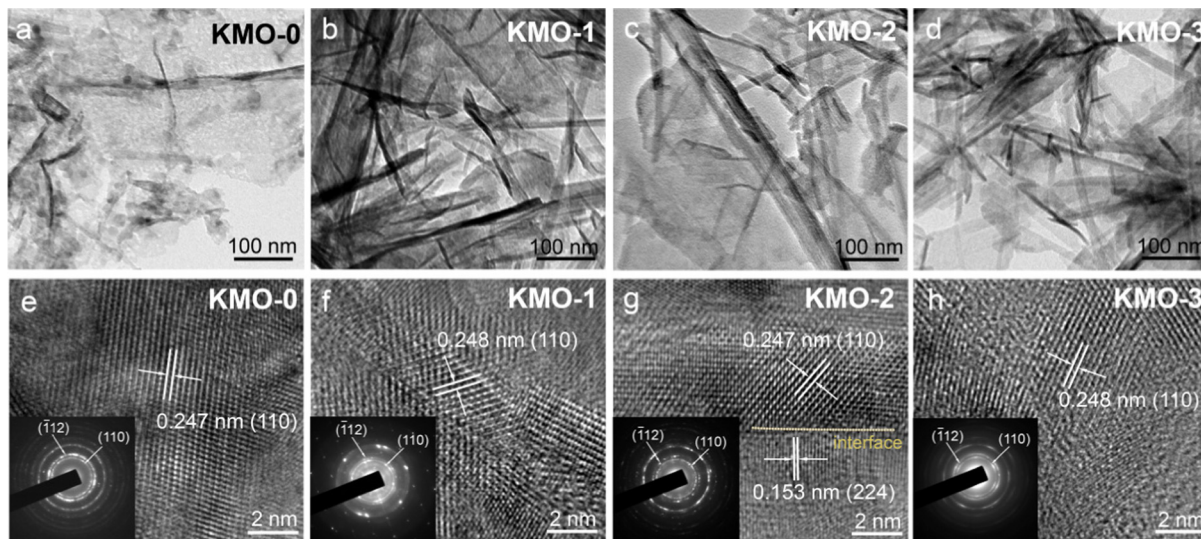


Fig. 3 (a–d) TEM images of the KMO–KMO-3 samples. (e–h) HRTEM images of the KMO–KMO-3 samples (insets show the SAED patterns).

the (224) plane of Mn_3O_4 , respectively, and an obvious hetero-junction is generated in the middle region (Fig. 3g). Therefore, the birnessite/ Mn_3O_4 heterostructure is fabricated *via* the two-step hydrothermal reaction. The SAED pattern and TEM image of Mn_3O_4 nanowires in the KMO-2 sample are displayed in Fig. S5 (ESI[†]) to further validate that the generated nanowires are spinel Mn_3O_4 .

The K^+ storage performances of the KMO–KMO-3 samples in K_2SO_4 aqueous electrolyte were investigated using cyclic voltammetry (CV) and galvanostatic measurements in the potential range of 0–1.1 V (*vs.* SCE), with the results presented in Fig. 4. Fig. 4a shows the cyclic voltammetry curves of KMO, KMO-1, KMO-2 and KMO-3 at 0.3 mV s^{-1} . For the KMO electrode, the CV curve exhibits a typical pseudocapacitive characteristic, and a pair of wide redox peaks (1.0 V/0.93 V *vs.* SCE) and a pair of weak peaks (0.58 V/0.4 V *vs.* SCE) are observed. After the two-step hydrothermal reaction, three pronounced oxidation peaks appear at around 0.37 V, 0.59 V, and 1.05 V (*vs.* SCE) in the CV curves of KMO-1–KMO-3 electrodes, accompanied by two reduction peaks at around 0.34 V and 1.0 V. These redox peaks after the secondary hydrothermal reaction become more pronounced, indicating enhanced K^+ insertion/extraction in the layered/spinel heterostructure. Fig. S6 (ESI[†]) shows the initial three cycles of cyclic voltammetry curves for KMO–KMO-3 at a scan rate of 0.3 mV s^{-1} . It can be seen that mainly four oxidation peaks are located at 0.40 V, 0.59 V, 0.78 V, and 1.05 V, respectively, during the first cycle for KMO-1, KMO-2 and KMO-3. The peak current intensity of KMO-2 is obviously higher than those of other samples and exhibits better reversibility. The galvanostatic charge–discharge curves at 100 mA g^{-1} of the four samples are shown in Fig. 4b. According to eqn (S1) (ESI[†]), the calculated capacity of KMO, KMO-1, KMO-2 and KMO-3 is 106 mA h g^{-1} , 112 mA h g^{-1} , 147 mA h g^{-1} and 99 mA h g^{-1} at 100 mA g^{-1} , respectively. The galvanostatic charge/discharge curves of the KMO–KMO-3 electrodes at various current densities of 50–2000 mA g^{-1} are

presented in Fig. S7 (ESI[†]). The four samples all display high coulombic efficiency and good reversibility. However, the capacity of KMO-3 with a higher K content electrode decreased significantly, which can be attributed to too high content of Mn_3O_4 and rare heterogeneous interfaces in the KMO-3 electrode. The K-storage performance of the Mn_3O_4 electrode in saturated K_2SO_4 electrolyte was investigated, as shown in Fig. S8 (ESI[†]). After the two-step hydrothermal reaction for 960 min, the material is basically converted to Mn_3O_4 according to the XRD pattern (Fig. S1[†]). The CV curves and charge/discharge curves of spinel Mn_3O_4 exhibit typical pseudocapacitive characteristics during the potassium storage process, and its capacity (51 mA h g^{-1} at 50 mA g^{-1}) is obviously lower than that of the layered birnessite electrode. Hence, with an increase in the second-step hydrothermal reaction time, the increased K content in birnessite is beneficial for improved capacity, but consequent higher Mn_3O_4 content in the composite electrode would drag down the average capacity. Fig. S8d (ESI[†]) displays the cyclic stability of Mn_3O_4 for 2000 cycles at 1 A g^{-1} . Even after 2000 cycles, Mn_3O_4 still retains 95% capacity retention, indicating that the heterostructure plays an important role in the enhanced K^+ storage capability. The charge/discharge specific capacities of KMO–KMO-3 electrodes at different current densities as a function of cycle number are compared in Fig. 4c. When the current density increased from 50 to 2000 mA g^{-1} , the capacity retention of KMO-0, KMO-2, KMO-1 and KMO-3 is 32%, 63%, 48% and 55%, respectively. Based on Mo's theoretical study, increasing K content can lead to faster K^+ ion diffusion because of the concerted ionic diffusion behavior of multiple ions with low energy barriers.⁴⁵ Therefore, the KMO-2 electrode with a heterostructure composed of birnessite with high K content and the Mn_3O_4 phase exhibits the best rate capability with fast K^+ intercalation/deintercalation. The cyclic stabilities of the KMO–KMO-3 samples are further compared in Fig. 4d. After 1000 charge/discharge cycles at a current density of 1 A g^{-1} , the KMO, KMO-1, KMO-2, and KMO-3 electrode



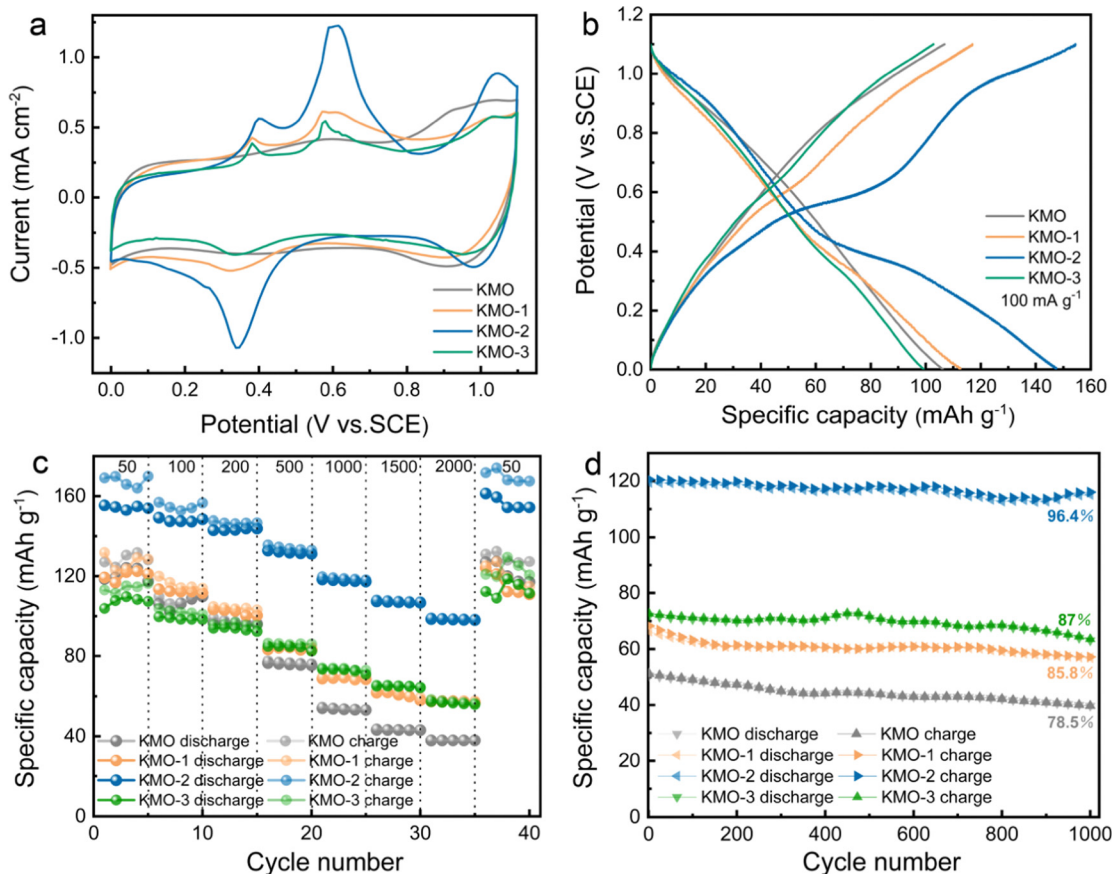


Fig. 4 (a) CV curves of the KMO–KMO-3 samples at a scan rate of 0.3 mV s^{-1} . (b) Charge/discharge curves of the KMO–KMO-3 samples at a current density of 100 mA g^{-1} . (c) Rate capabilities of the KMO–KMO-3 electrodes. (d) Cyclic performances of the KMO–KMO-3 samples at 1 A g^{-1} for 1000 cycles.

retain 78.5%, 85.8%, 96.4% and 87% capacity retention, respectively, indicating that KMO-2 exhibits excellent cyclic stability.

The electrochemical kinetics of KMO–KMO-3 electrodes was investigated to further explain their superior rate performance. Fig. S9 (ESI[†]) presents the CV curves for the four samples at different scan rates ranging from 0.1 to 5 mV s^{-1} . The $\log(i)$ versus $\log(\nu)$ plot for the cathodic and anodic peaks shows the current dependence on the scan rate. A b value of 0.5 indicates that the current is controlled by semiinfinite diffusion while $b = 1$ indicates capacitive behaviour. For the four samples, the b value is in the range of 0.5 – 1 , indicating that the material capacity is the contribution of diffusion-controlled capacity and the surface capacitance together. *Via* the CV curves, the capacitance-control and diffusion-control capacitance can be calculated accurately through eqn (S2) and (S3) (ESI[†]) by quantitative analysis. In addition, the b value of the KMO-2 electrode is lower than those of other electrodes (Fig. S9, ESI[†]), which may be ascribed to more intercalation of K^+ into the internal hetero-interface. The capacitive contribution process turns into more dominant gradually upon the increased scan rate, which can be explained by the rapid capacitive behaviour of potassium ion storage at the electrode surface. Fig. S10 (ESI[†]) shows that the capacitive-controlled contribution of KMO-2 is

65% *via* the CV curve at 0.3 mV s^{-1} , proving the fast reaction kinetics.^{52,53}

As displayed in Fig. 5a, the first loop and fifth loop curves of KMO-2 nearly overlap, implying a good reversibility. After the 25th charge/discharge cycle, the KMO-2 electrode delivers a reversible capacity of 119 mA h g^{-1} at a high current density of 1 A g^{-1} . The long-term cyclic stability of the KMO-2 electrode was further determined at 1 A g^{-1} (Fig. 5b). KMO-2 maintains 91.7% initial capacity after 2000 cycles and the coulombic efficiency is close to 99% during the charge/discharge process, revealing both excellent structural stability and high reversibility. Compared with recently reported electrode materials in APIs, as shown in Table S5 (ESI[†]), the prepared KMO-2 electrode outperforms most of the APIB cathodes and exhibits superior K-storage performance and rate capability. After 2000 charge/discharge cycles, the charge/discharge platform does not become obvious and the capacity decreases slightly. To explore the reason for good stability of KMO-2 electrode, the XRD spectra of KMO-2 after cycling was analyzed. Fig. 5c exhibits that the peak intensities of the (001) and (002) planes reduce significantly after 2000 charge/discharge cycles, suggesting that the heterostructure tends to be amorphous. According to the previous research work,⁴¹ the amorphous phase is conducive to the transport of ions within the bulk phase and



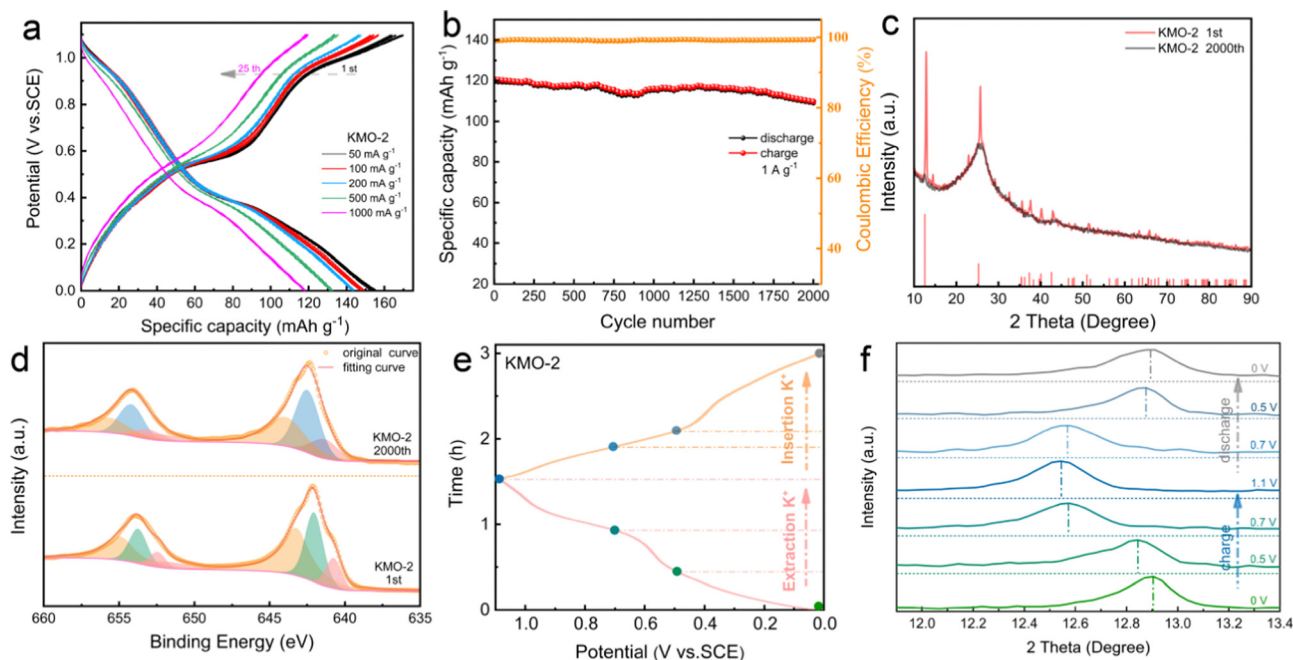


Fig. 5 (a) The galvanostatic charge/discharge profiles of the KMO-2 electrode at different current densities from the 1st cycle to the 25th cycle. (b) Long-term cyclic stability and corresponding coulombic efficiency of the KMO-2 sample at 1 A g^{-1} for 2000 cycles. (c) The XRD patterns and (d) the XPS spectra of the KMO-2 electrode after the 1st cycle and after 2000 cycles, respectively. (e) Charge/discharge curve of the KMO-2 sample at 20 mA g^{-1} . (f) *Ex situ* XRD patterns of the KMO-2 sample upon the second cycle.

increases the electron conductivity. Compared with the crystal material, the ion diffusion in the amorphous phase is greatly improved. In Fig. 5d, the XPS spectra of the Mn 2p orbital after long-term cycling shows that the Mn^{4+} content decreased by 9.5%, due to the irreversible K-ion intercalation/deintercalation which is the main reason for capacity fade. The outstanding K^+ storage capability of the KMO-2 heterostructure electrode is probably owing to its reversible structural changes during the depotassiation/potassiation process. To verify this speculation, *ex situ* XRD was performed upon the second charging/discharging as shown in Fig. 5e and f. The (001) peak shifted significantly to a lower angle direction upon charging to 1.1 V (Fig. 5e), which is commonly observed in layered cathodes for rechargeable batteries, indicating the increasing interplanar space due to the enhanced coulombic repulsion between the MnO_6 slabs upon K^+ extraction. The (001) interplanar spacing overall continuously increases and reduces upon depotassiation and potassiation. The reversible peak shift of the (001) plane suggests a reversible K^+ exchange in the heterostructure electrode during the charge/discharge.

To elucidate the mechanism of the K^+ storage in the heterostructure, the densities of states in the birnessite, spinel Mn_3O_4 and heterostructure electrodes were investigated by first-principles computation. As displayed in Fig. 6a, compared with the energy band structures of birnessite and Mn_3O_4 , the heterostructure shows obvious metallic characteristics, as the band gap is 0 eV. The birnessite and spinel Mn_3O_4 has a band gap of 1.79 eV and 0.60 eV, respectively. In general, the wider band gap means worse electrical conductivity that results in more difficult electron transfer. This result implies that the

heterostructure composed of birnessite and Mn_3O_4 improves the electronic conductivity. Nevertheless, the practical use of Mn-based oxide cathodes in APBs has been hindered by the synergistic Jahn–Teller effect associated with high spin Mn^{3+} , which leads to severe structural degradation and rapid capacity decay. In Fig. 6b, single-electron occupation in the double-degenerate e_g level results in a local Jahn–Teller distortion, with the Mn–O bonds elongated along one octahedral axis.⁵⁰ For a detailed description of the electronic structure, Fig. 6c shows the Mn d_{z^2} density of states of birnessite, spinel Mn_3O_4 and heterostructure, respectively. A significant change can be observed in the density of states for the heterostructure, which moves above the Fermi level. The heterostructures of birnessite and spinel Mn_3O_4 lead to redistribution of the Mn 3d state, which may provide more electrons to participate in the 3d state of manganese atoms at the bottom of the conduction band. The charge compensation effect between Mn and O reduces the transition energy of electrons from the valence band to the conduction band. As a result, the electron rearrangement in the 3d state of manganese atoms in the heterostructure can disturb the long-range order of the original d_{z^2} orbital in birnessite or spinel Mn_3O_4 , effectively suppressing the Jahn–Teller effect and maintaining long lifetime of the electrode. After geometric optimization for the interface formed by birnessite and Mn_3O_4 , it is found that the O atoms of birnessite tend to bind with the Mn atoms of Mn_3O_4 , as shown in Fig. 6d, which will also contribute to the strong binding force between birnessite and Mn_3O_4 . Moreover, the Gibbs free energy calculations show that K^+ adsorption energy decreases after introducing Mn_3O_4 . For the heterostructure, the Gibbs free energy of K-ion



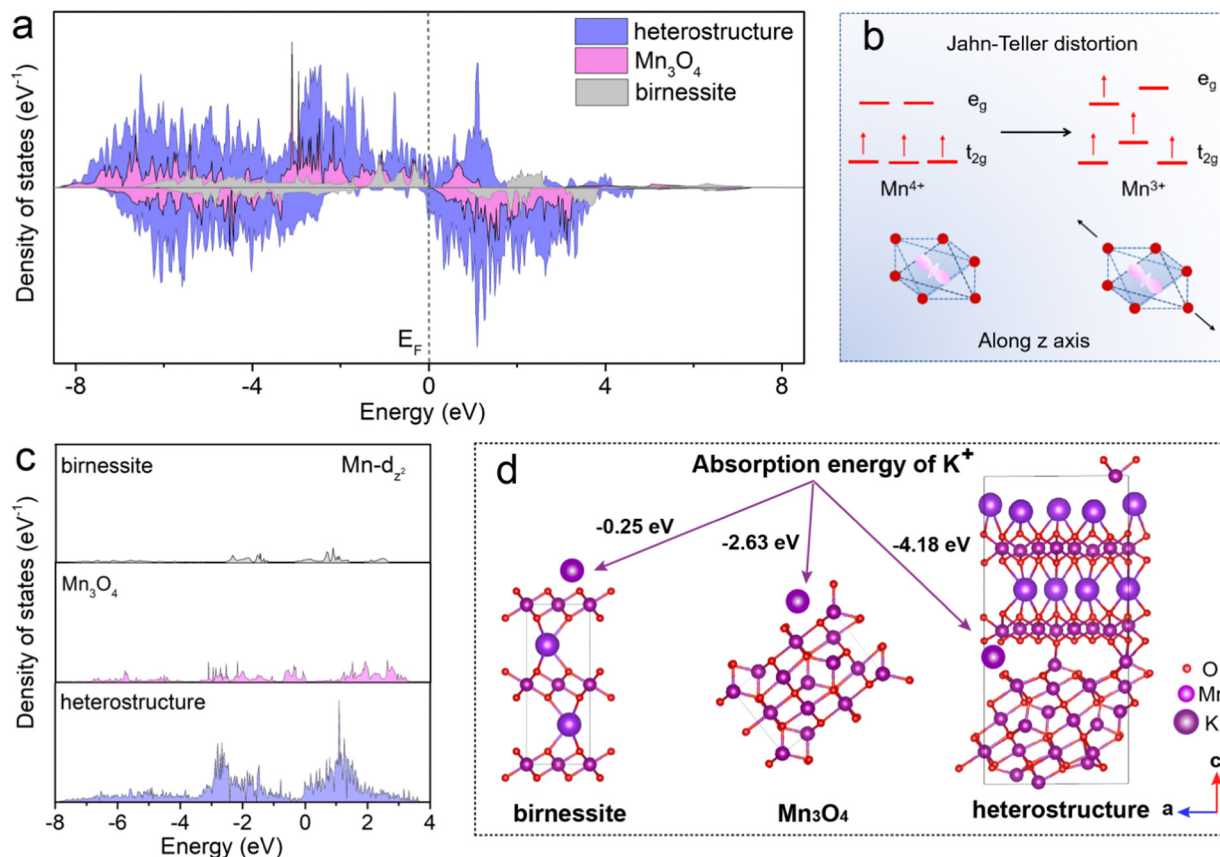


Fig. 6 (a) The birnessite, Mn_3O_4 and heterostructure model structures corresponding to the state density. The dashed gray line is the Fermi energy (E_F). (b) Splitting of the e_g levels of d orbitals in an octahedral environment caused by Jahn–Teller distortion. (c) Partial density of states of Mn- d_{z^2} in the birnessite, Mn_3O_4 and heterostructure. (d) Calculated absorption energies for K^+ on the surfaces of perfect birnessite, Mn_3O_4 and heterostructure model structures.

adsorption is -4.18 eV, which is significantly lower than the Gibbs free energy of K ions on the birnessite (-0.25 eV) and spinel Mn_3O_4 (-2.63 eV). The lower Gibbs adsorption energy of the heterostructure indicates the larger electrochemical active surface area for the adsorption, induced by heterogeneous interface effects. The more active sites from the heterostructure can absorb more potassium ions and promote the surface kinetics, resulting in high rate capacity.

4. Conclusions

In summary, a Mn-based oxide heterostructure composed of birnessite $\text{K}_{0.52}\text{MnO}_2 \cdot 0.22\text{H}_2\text{O}$ and spinel Mn_3O_4 is fabricated *via* a facile two-step hydrothermal reaction, as the high-performance cathode for AIBs. The optimized birnessite/spinel heterostructure delivers a high specific capacity of 147 mA h g^{-1} at a current density of 100 mA g^{-1} , as well as superior cycling stability at 91.7% capacity retention after 2000 cycles. We discovered that the layered birnessite/spinel Mn_3O_4 heterostructure can stabilize the electrode structure and relieve Mn dissolution, as elucidated by *ex situ* XRD and DFT calculations. This work provides a promising strategy for interface engineering and effective heterostructure design and

for promoting the development of Mn-based cathodes for high-performance aqueous potassium-ion batteries.

Author contributions

Zheng Guan: conceptualization, data acquisition and analysis, methodology, original draft preparation, writing – original draft. Yunan Wang: investigation, formal analysis, methodology, writing – review & editing. Mingyue Zhang: validation, investigation. Jie Liu: methodology, investigation. Shuangwen Li: funding acquisition, resources. Di Guo: project administration, supervision, writing – review & editing. Xiaoxia Liu: funding acquisition, supervision, writing – review & editing.

Conflicts of interest

The authors declare no conflict of interest.

Acknowledgements

S. W. L. acknowledges the financial support from the National Natural Science Foundation of China (52003007). X.-X. L. is grateful for the financial support from the Liaoning Science



and Technology Development Foundation Guided by Central Government (2021JH6/10500139). The authors thank Xinli Wang from the Analytical and Testing Center of Northeastern University for TEM data acquisition.

Notes and references

- N. Kittner, F. Lill and D. M. Kammen, *Nat. Energy*, 2017, **2**, 1–6.
- C. Zhang, Y. L. Wei, P. F. Cao and M. C. Lin, *Renewable Sustainable Energy Rev.*, 2018, **82**, 3091–3106.
- T. M. Gur, *Energy Environ. Sci.*, 2018, **11**, 2696–2767.
- W. Zhang, Y. Dai, R. Chen, Z. Xu, J. Li, W. Zong, H. Li, Z. Li, Z. Zhang, J. Zhu, F. Guo, X. Gao, Z. Du, J. Chen, T. Wang, G. He and I. P. Parkin, *Angew. Chem., Int. Ed.*, 2023, **62**, e202212695.
- W. Zhang, Y. Wu, Z. Xu, H. Li, M. Xu, J. Li, Y. Dai, W. Zong, R. Chen, L. He, Z. Zhang, D. J. L. Brett, G. He, Y. Lai and I. P. Parkin, *Adv. Energy Mater.*, 2022, **12**, 2201065.
- R. Chen, H. Tang, Y. Dai, W. Zong, W. Zhang, G. He and X. Wang, *ACS Nano*, 2022, **16**, 19124–19132.
- J. O. G. Posada, A. J. R. Rennie, S. P. Villar, V. L. Martins, J. Marinaccio, A. Barnes, C. F. Glover, D. A. Worsley and P. J. Hall, *Renewable Sustainable Energy Rev.*, 2017, **68**, 1174–1182.
- H. S. Ao, Y. Y. Zhao, J. Zhou, W. L. Cai, X. T. Zhang, Y. C. Zhu and Y. T. Qian, *J. Mater. Chem. A*, 2019, **7**, 18708–18734.
- D. L. Chao, W. H. Zhou, F. X. Xie, C. Ye, H. Li, M. Jaroniec and S. Z. Qiao, *Sci. Adv.*, 2020, **6**, eaba4098.
- Q. Q. Yao and C. B. Zhu, *Adv. Funct. Mater.*, 2020, **30**, 2005209.
- A. Eftekhari, Z. L. Jian and X. L. Ji, *ACS Appl. Mater. Interfaces*, 2017, **9**, 4404–4419.
- B. Wang, E. H. Ang, Y. Yang, Y. F. Zhang, M. H. Ye, Q. Liu and C. C. Li, *Chem. – Eur. J.*, 2021, **27**, 512–536.
- M. F. Zhou, P. X. Bai, X. Ji, J. X. Yang, C. S. Wang and Y. H. Xu, *Adv. Mater.*, 2021, **33**, 2003741.
- L. W. Jiang, Y. X. Lu, C. L. Zhao, L. L. Liu, J. N. Zhang, Q. Q. Zhang, X. Shen, J. M. Zhao, X. Q. Yu, H. Li, X. J. Huang, L. Q. Chen and Y. S. Hu, *Nat. Energy*, 2019, **4**, 495–503.
- K. Kubota, M. Dahbi, T. Hosaka, S. Kumakura and S. Komaba, *Chem. Rec.*, 2018, **18**, 459–479.
- Q. Zhang, Z. Wang, S. Zhang, T. Zhou, J. Mao and Z. Guo, *Electrochem. Energy Rev.*, 2018, **1**, 625–658.
- J. Y. Hwang, S. T. Myung and Y. K. Sun, *Adv. Funct. Mater.*, 2018, **28**, 1802938.
- H. Kim, J. C. Kim, M. Bianchini, D. H. Seo, J. Rodriguez-Garcia and G. Ceder, *Adv. Energy Mater.*, 2018, **8**, 1702384.
- W. C. Zhang, Y. J. Liu and Z. P. Guo, *Sci. Adv.*, 2019, **5**, eaav7412.
- V. D. Neff, *J. Electrochem. Soc.*, 1978, **125**, 886.
- M. Pasta, C. D. Wessells, R. A. Huggins and Y. Cui, *Nat. Commun.*, 2012, **3**, 1–7.
- D. W. Su, A. McDonagh, S. Z. Qiao and G. X. Wang, *Adv. Mater.*, 2017, **29**, 1604007.
- D. S. Charles, M. Feyngenson, K. Page, J. Neufeind, W. Q. Xu and X. W. Teng, *Nat. Commun.*, 2017, **8**, 1–8.
- W. Ren, X. Chen and C. Zhao, *Adv. Energy Mater.*, 2018, **8**, 1801413.
- J. Ge, L. Fan, A. M. Rao, J. Zhou and B. Lu, *Nat. Sustainability*, 2022, **5**, 225–234.
- M. T. Xia, X. K. Zhang, T. T. Liu, H. X. Yu, S. Chen, N. Peng, R. T. Zheng, J. D. Zhang and J. Shu, *Chem. Eng. J.*, 2020, **394**, 124923.
- M. T. Wang, H. Q. Wang, H. M. Zhang and X. F. Li, *J. Energy Chem.*, 2020, **48**, 14–20.
- K. J. Zhu, Z. P. Li, T. Jin and L. F. Jiao, *J. Mater. Chem. A*, 2020, **8**, 21103–21109.
- R. Chua, Y. Cai, Z. K. Kou, R. Satish, H. Ren, J. J. Chan, L. P. Zhang, S. A. Morris, J. M. Bai and M. Srinivasan, *Chem. Eng. J.*, 2019, **370**, 742–748.
- X.-Z. Zhai, J. Qu, S.-M. Hao, Y.-Q. Jing, W. Chang, J. Wang, W. Li, Y. Abdelkrim, H. Yuan and Z.-Z. Yu, *Nano-Micro Lett.*, 2020, **12**, 1–15.
- C. Vaalma, G. A. Giffin, D. Buchholz and S. Passerini, *J. Electrochem. Soc.*, 2016, **163**, A1295–A1299.
- B. W. Lin, X. H. Zhu, L. Z. Fang, X. Y. Liu, S. Li, T. Zhai, L. Xue, Q. B. Guo, J. Xu and H. Xia, *Adv. Mater.*, 2019, **31**, 1900060.
- Q. Zhang, C. Didier, W. K. Pang, Y. J. Liu, Z. J. Wang, S. Li, V. K. Peterson, J. F. Mao and Z. P. Guo, *Adv. Energy Mater.*, 2019, **9**, 1900568.
- Y. Z. Liu, Z. M. Qin, X. P. Yang and X. Q. Sun, *Adv. Funct. Mater.*, 2022, **32**, 2106994.
- L. Q. Mai, J. Z. Sheng, L. Xu, S. S. Tan and J. S. Meng, *Acc. Chem. Res.*, 2018, **51**, 950–959.
- S. Z. Huang, Z. H. Wang, Y. V. Lim, Y. Wang, Y. Li, D. H. Zhang and H. Y. Yang, *Adv. Energy Mater.*, 2021, **11**, 2003689.
- W. J. Hyun, C. M. Thomas, N. S. Luu and M. C. Hersam, *Adv. Mater.*, 2021, **33**, 2007864.
- P. Xiong, Y. Y. Wu, Y. F. Liu, R. Z. Ma, T. Sasaki, X. Wang and J. W. Zhu, *Energy Environ. Sci.*, 2020, **13**, 4834–4853.
- Y. Y. Wang, D. Liu, M. L. Sun and J. P. Liu, *Mater. Chem. Front.*, 2021, **5**, 7384–7402.
- N. Zhang, F. Y. Cheng, J. X. Liu, L. B. Wang, X. H. Long, X. S. Liu, F. J. Li and J. Chen, *Nat. Commun.*, 2017, **8**, 1–9.
- R. Z. Zhao, H. X. Di, X. B. Hui, D. Y. Zhao, R. T. Wang, C. X. Wang and L. W. Yin, *Energy Environ. Sci.*, 2020, **13**, 246–257.
- W. J. Hyun, C. M. Thomas, N. S. Luu and M. C. Hersam, *Adv. Mater.*, 2021, **33**, 2007864.
- L. N. Zhao, G. R. Chen, Y. H. Weng, T. T. Yan, L. Y. Shi, Z. X. An and D. S. Zhang, *Chem. Eng. J.*, 2020, **401**, 126138.
- H. Y. Shi, Y. Song, Z. M. Qin, C. C. Li, D. Guo, X. X. Liu and X. Q. Sun, *Angew. Chem., Int. Ed.*, 2019, **58**, 16057–16061.
- H. Z. Lv, Y. Song, Z. M. Qin, M. Y. Zhang, D. Yang, Q. Pan, Z. H. Wang, X. J. Mu, J. M. Meng, X. Q. Sun and X. X. Liu, *Chem. Eng. J.*, 2022, **430**, 133064.
- X. F. He, Y. Z. Zhu and Y. F. Mo, *Nat. Commun.*, 2017, **8**, 1–7.
- Y. Zou, A. Dong, Z. Guo, L. Ye, Y. Cui, M. Guo, L. Zhao and Q. Jiang, *ACS Appl. Nano Mater.*, 2020, **3**, 5612–5624.



- 48 L. L. Fan, Z. H. Li, W. M. Kang and B. W. Cheng, *J. Energy Chem.*, 2021, **55**, 25–33.
- 49 F. F. Liu, S. Jin, Q. X. Xia, A. G. Zhou and L. Z. Fan, *J. Energy Chem.*, 2021, **62**, 220–242.
- 50 X. H. Zhu, F. Q. Meng, Q. H. Zhang, L. Xue, H. Zhu, S. Lan, Q. Liu, J. Zhao, Y. H. Zhuang, Q. B. Guo, B. Liu, L. Gu, X. Lu, Y. Ren and H. Xia, *Nat. Sustainability*, 2021, **4**, 392.
- 51 Y. Li, J. W. Zhang, Q. G. Chen, X. H. Xia and M. H. Chen, *Adv. Mater.*, 2021, **33**, 2100855.
- 52 Y. Jiang and J. Liu, *Energy Environ. Mater.*, 2019, **2**, 30–37.
- 53 W. Zhang, Z. Xu, H. Li, M. Xu, S. Wang, Z. Li, A. Wang, L. Zhang, L. He, S. Li, B. Zhu, Z. Zhang and Y. Lai, *Chem. Eng. J.*, 2022, **433**, 133542.

